NEUROSCIENCE

Interregional synaptic maps among engram cells underlie memory formation

Jun-Hyeok Choi,* Su-Eon Sim,* Ji-il Kim,* Dong Il Choi,* Jihae Oh, Sanghyun Ye, Jaehyun Lee, TaeHyun Kim, Hyoung-Gon Ko, Chae-Seok Lim, Bong-Kiun Kaang†

Memory resides in engram cells distributed across the brain. However, the site-specific substrate within these engram cells remains theoretical, even though it is generally accepted that synaptic plasticity encodes memories. We developed the dual-eGRASP (green fluorescent protein reconstitution across synaptic partners) technique to examine synapses between engram cells to identify the specific neuronal site for memory storage. We found an increased number and size of spines on CA1 engram cells receiving input from CA3 engram cells. In contextual fear conditioning, this enhanced connectivity between engram cells encoded memory strength. CA3 engram to CA1 engram projections strongly occluded long-term potentiation. These results indicate that enhanced structural and functional connectivity between engram cells across two directly connected brain regions forms the synaptic correlate for memory formation.

Memory storage and retrieval require specific populations of neurons that show increased neuronal activity during memory formation. Several studies identified these engram cells throughout various brain regions and demonstrated that activated engram cells can induce artificial retrieval of stored memories (*1*–*6*). To explain how memory is encoded in the engram, Hebb proposed a hypothetical mechanism, often paraphrased as "fire together, wire together" (*7*). This hypothesis suggests that synaptic strengthening between coactivated neurons forms the neural substrate of memory. However, it has not been possible to delineate whether memory formation enhances synapses between engram cells in connected brain regions because we could not distinguish presynaptic regions originating from engram cells and nonengram cells.

To compare two different presynaptic populations that project to a single postsynaptic neuron, we modified the green fluorescent protein (GFP) reconstitution across synaptic partners (GRASP) technique (*8*, *9*). GRASP uses two complementary mutant GFP fragments (*10*), which are expressed separately on presynaptic and postsynaptic membranes and reconstitute in the synaptic cleft to form functional GFP. This GFP signal indicates a formed synapse between the neuron expressing the presynaptic component and the neuron expressing the postsynaptic component. We developed an enhanced GRASP (eGRASP) technique, which exhibits increased GRASP signal intensity by introducing a weakly interacting domain that facilitates GFP reconstitution and a single mutation commonly found on most advanced GFP variants (fig. S1) (*11*). We further evolved eGRASP to reconstitute cyan or yellow fluorescent protein (Fig. 1, A and B, and fig. S2) (*12*–*14*). Placing the color-determining domain in the presynaptic neuron (cyan/yellow pre-eGRASP) and the common domain to the postsynaptic neuron (post-eGRASP) enabled visualization of the two synaptic populations that originated from two different presynaptic neuron populations and projected to a single postsynaptic neuron. We named this technique dual-eGRASP (Fig. 1A). We demonstrated that two colors reveal the contact interface in human embryonic kidney (HEK) 293T cells expressing the common domain with cells expressing either of the color-determining domains (Fig. 1C). We successfully applied this technique to synapses on dentate gyrus (DG) granule cells originating from either the lateral entorhinal cortex (LEC) or the medial entorhinal cortex (MEC) that projected to the outer and middle molecular layers of the DG, respectively (Fig. 1D) (*15*). This technique can also separately label intermixed synapses that do not have a unique spatial distribution on CA1 pyramidal neurons that originate from either the contralateral CA3 or ipsilateral CA3 (Fig. 1E) (*16*). We confirmed that the eGRASP formation itself does not induce undesired strengthening of the synaptic transmission between the neurons expressing pre-eGRASP and post-eGRASP (fig. S3).

To apply dual-eGRASP on synaptic connections between engram cells from two different regions, we used a Fos promoter–driven reverse tetracycline–controlled transactivator (rtTA) delivered by adeno-associated virus (AAV) to express specific genes of interest in the engram cells at particular time points (*17*–*20*). Doxycycline injection 2 hours before either seizure induction or contextual fear conditioning (CFC) successfully labeled the cells activated during these events (figs. S4 and S5). Using this Fos-rtTA system, we expressed post-eGRASP together with membrane-targeted mScarlet-I (*21*) unilaterally in CA1 engram cells and yellow pre-eGRASP in the contralateral CA3 engram cells to avoid possible coexpression of pre-eGRASP and post-eGRASP. This system labeled CA3 engram to CA1 engram (E-E) synapses with yellow eGRASP signals on red fluorescently labeled dendrites. To compare these synapses with other synapses [nonengram to engram (N-E), engram to nonengram (E-N), and nonengram to nonengram (N-N) synapses], we expressed post-eGRASP together with membrane-targeted iRFP670 (*22*) in a sparse neuronal population from the ipsilateral CA1, while expressing cyan pre-eGRASP in a random neuronal population from the contralateral CA3. We achieved strong expression in the random neuronal population using a high titer of double-floxed inverted open reading frame (DIO) AAV with a lower titer of Cre recombinase expressing AAV (Fig. 2A). We confirmed that yellow pre-eGRASP expression is doxycycline dependent, demonstrating that this system can label synapses originating from engram cells of a specific event (fig. S6). We successfully distinguished four types of synapses in the same brain slice after CFC. Based on the percentage of overlapping fluorescence, CA3 cells expressing cyan pre-eGRASP, yellow pre-eGRASP, CA1 cells expressing iRFP and mScarlet-I are estimated to be 78.38, 40.25, 11.61, and 20.93%, respectively (fig. S7). Cyan and yellow puncta on red (mScarlet-I) dendrites indicated N-E and E-E synapses, respectively, whereas cyan and yellow puncta on near-infrared (iRFP670) dendrites indicated N-N and E-N synapses (Fig. 2, B and C). We considered puncta expressing both cyan and yellow fluorescence as synapses originating from engram cells, because these synapses originate from CA3 cells expressing both cyan pre-eGRASP (randomly selected population) and yellow pre-eGRASP (engram cells). We found no significant differences between the density of N-N and N-E synapses (Fig. 2D and fig. S8, A and C); however, the density of E-E synapses was significantly higher than E-N synapses (Fig. 2D and fig. S8, B and D). This difference indicates that presynaptic terminals from CA3 engram cells predominantly synapsed on CA1 engram cells rather than CA1 nonengram cells. We also examined the size of spines in each synapse population. E-E spine head diameter and spine volume were significantly greater than N-E synaptic spines, whereas N-N and E-N did not show any significant differences (Fig. 2E).

Although the number of engram cells may remain constant across different memory strengths (*23*), we predicted that connectivity between pre- and post-engram cells could encode memory strength. We investigated whether memory strength correlates with connectivity between engram cells using the same combination of

School of Biological Sciences, Seoul National University, Gwanak-gu, Seoul 08826, South Korea.
*These authors contributed equally to this work.
†Corresponding author. Email: kaang@snu.ac.kr

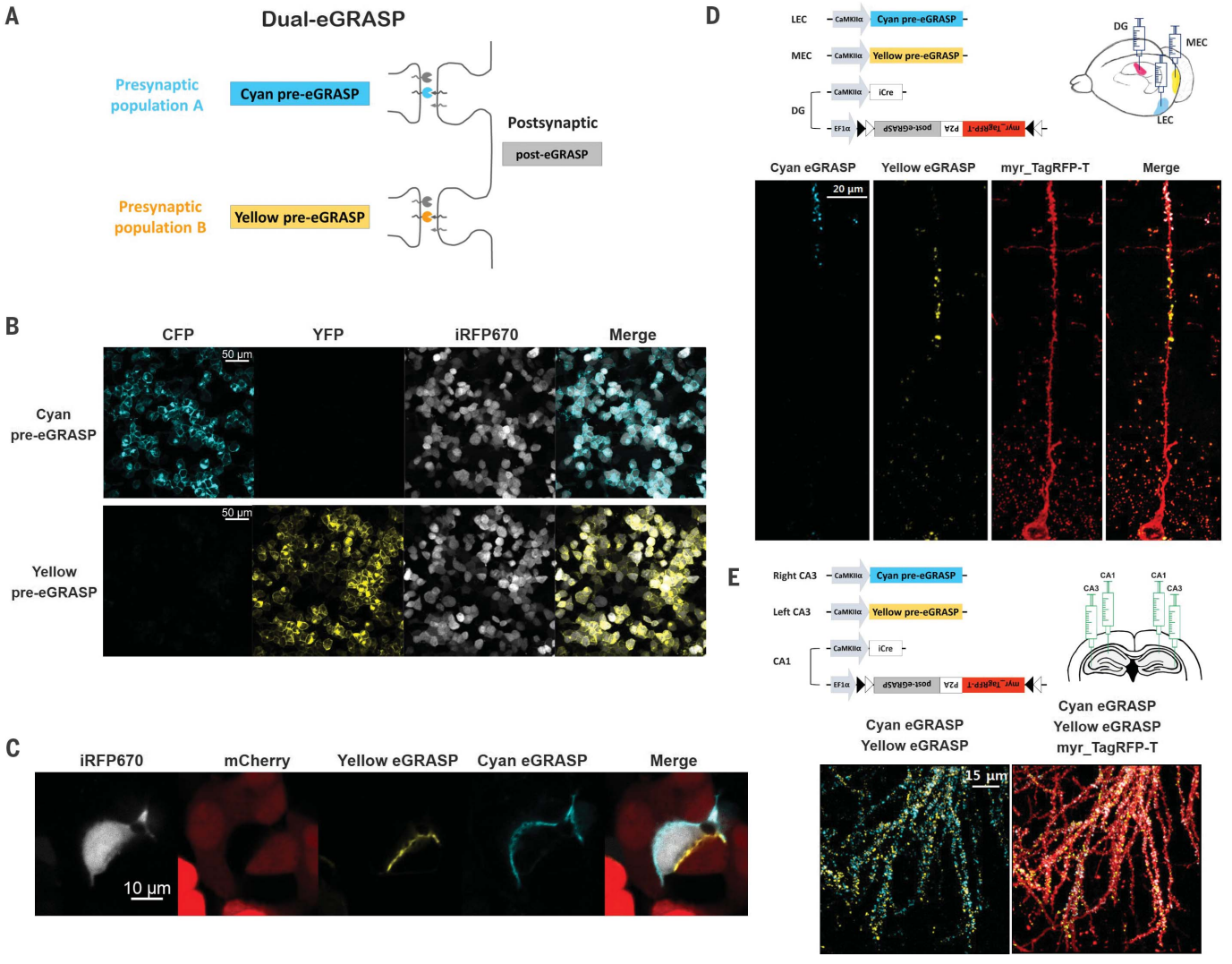

Fig. 1. Dual-eGRASP differentiates two population of synapses on a single neuron. (**A**) Schematic illustration of cyan and yellow eGRASP. Cyan pre-eGRASP and yellow pre-eGRASP are expressed in two different presynaptic population, and common post-eGRASP is expressed in a single postsynaptic cell. (**B**) Coexpression of either cyan or yellow pre-eGRASP with post-eGRASP and iRFP670 in HEK293T cells. (**C**) Three populations of HEK293T cells were separately transfected using nucleofection. One population expressed cyan pre-eGRASP and mCherry, another population expressed yellow pre-eGRASP and mCherry, and the third population expressed post-eGRASP and iRFP670. (**D**) Cyan pre-eGRASP and yellow pre-eGRASP were expressed in the LEC and MEC, respectively. Post-eGRASP was expressed together with myristoylated TagRFP-T (myr_TagRFP-T) in the DG. (**E**) Cyan pre-eGRASP and yellow pre-eGRASP were expressed in the right CA3 and left CA3, respectively. Post-eGRASP was expressed together with myr_TagRFP-T in CA1.

AAVs and injection sites (Fig. 3A) as described in Fig. 2. To induce different strengths of memory, we divided mice into three groups. Mice were exposed to either weak (one shock of 0.35 mA) or strong (three shocks of 0.75 mA) electric foot shocks during CFC, while mice in the context-only group were exposed to the context without any foot shocks (Fig. 3B). Increasing electric foot shock intensity during memory formation produced higher freezing levels (Fig. 3C). When we quantified the number of CA3 and CA1 engram cells, we found no significant differences among the three groups (fig. S9) (*23*). There were no significant differences between the density of N-N and N-E synapses in all groups. However, we found a significantly higher density of E-E synapses in the strong shock group compared with the context only and weak shock group (Fig. 3, D and E). We further investigated whether the size of spines was positively correlated with memory strength. E-E spine head diameter and spine volume were significantly greater in the strong shock group than in the other groups, whereas N-N and E-N did not show any significant differences in all groups (Fig. 3F and fig. S10).

Because we found increased structural connectivity between CA3 and CA1 engram cells after memory formation, we investigated the synaptic strength of these synapses. We selectively stimulated two different inputs from CA3 neurons using two opsins, Chronos and ChrimsonR, that can be independently activated using blue and yellow wavelength lasers, respectively (*24*). We expressed ChrimsonR in CA3 engram neurons using Fos-rtTA, while we expressed Chronos primarily in CA3 excitatory neurons under the calcium/calmodulin-dependent protein kinase type II alpha (CaMKIIα) promoter (Fig. 4A) (*25*). We labeled CA1 engram neurons with nucleus-targeted mEmerald (mEmerald-Nuc) using Fos-rtTA and then performed whole-cell recordings from either CA1 engram or nonengram neurons. We investigated the following four combinations of synaptic responses in a single hippocampal slice after CFC: total excitatory to nonengram (T-N), total excitatory to engram (T-E), engram to nonengram (E-N), and engram to engram (E-E)

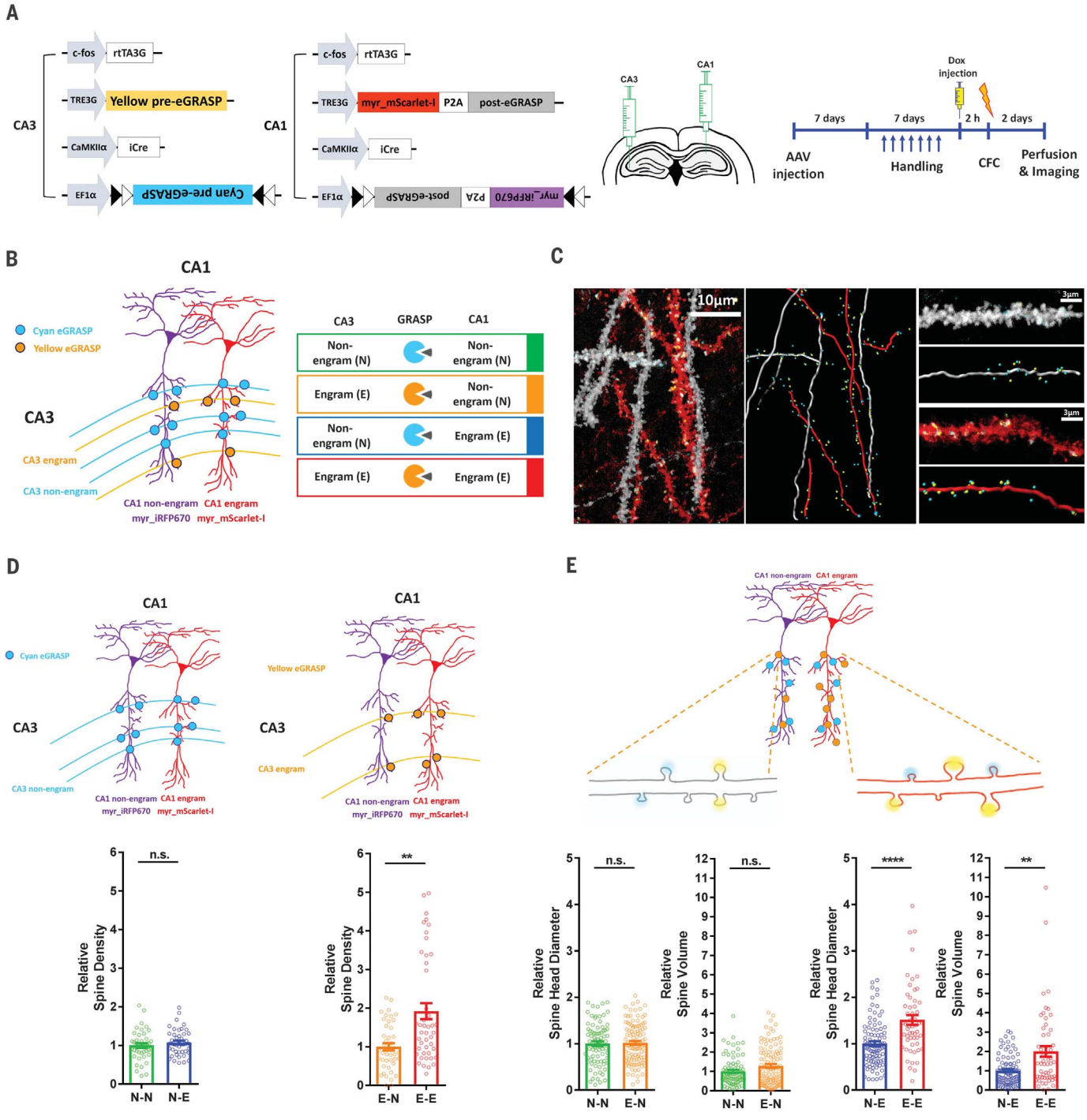

Fig. 2. CA3 engram to CA1 engram synapses exhibited higher synaptic density and larger spine size after memory formation. (**A**) (Left) Schematic illustration of injected AAVs. (Middle) Illustration of virus injection sites. Injection in each site was performed with a complete cocktail of all the virus infected in each site. (Right) Schematic of the experimental protocol. (**B**) (Left) Schematic diagram of the four possible synapse populations among engram and nonengram cells. (Right) Classification of the four synaptic populations indicated by four colors. Green, N-N; orange, E-N; blue, N-E; red, E-E. The color for each group applies to Figs. 2 and 3. (**C**) Representative image with three-dimensional modeling for analysis. (**D**) Normalized cyan/yellow eGRASP per dendritic length. The densities of cyan-only (left) or yellow puncta (right) on red dendrites are normalized to the corresponding cyan-only or yellow puncta on near-infrared dendrites from the same images in order to exclude the effect of different number of CA3 cells expressing each presynaptic components. Each data point represents a dendrite. $n = 43$ for CA1 nonengram dendrites; $n = 45$ for CA1 engram dendrites; 9 images from 3 mice. Mann Whitney two-tailed test. n.s., not significant; $^{**}P = 0.0017$. (**E**) Normalized spine head diameters and spine volumes of dendrites from CA1 nonengram cells (left) and engram cells (right) with schematic illustration. Sizes of the spines with yellow puncta were normalized to those of the spines with cyan-only puncta of the same dendrite. Each data point represents a spine. N-N, $n = 81$; E-N, $n = 107$; N-E, $n = 93$; E-E, $n = 55$. Mann Whitney two-tailed test. n.s., not significant; $^{**}P = 0.0014$; $^{****}P < 0.0001$. Data are represented as mean ± SEM.

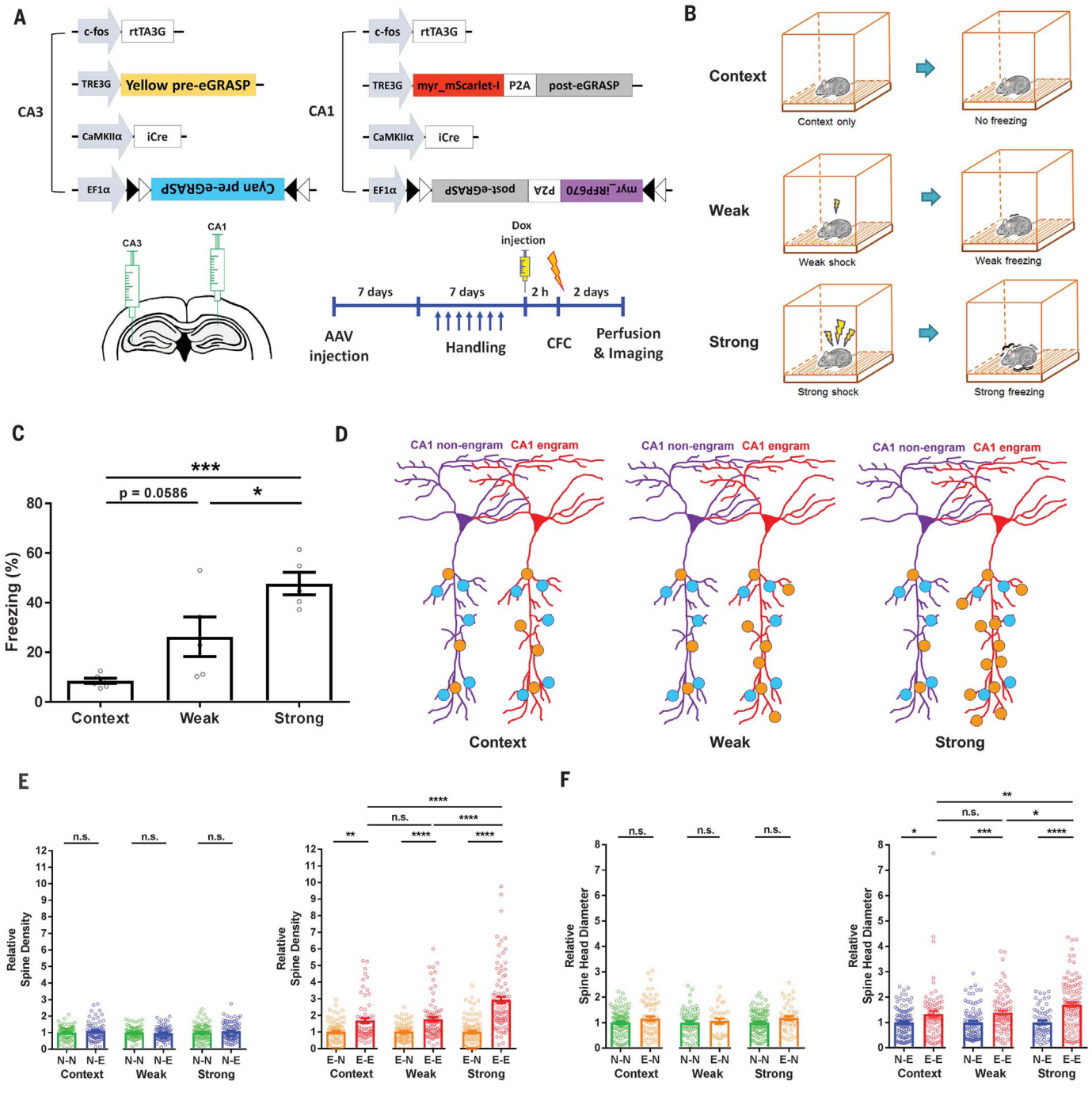

Fig. 3. Synaptic connectivity between pre- and post-engram cells is correlated to memory strength. (**A**) Schematic illustration of injected AAVs, illustration of virus injection sites, and experimental protocol. (**B**) Schematic illustration of the conditioning and retrieval process. (**C**) Freezing levels for each group: context, $n = 6$; weak, $n = 5$; strong, $n = 5$, Tukey's multiple comparison test after one-way analysis of variance (ANOVA); $F(2,13) = 15.85$; $^{*}P < 0.05$; $^{***}P < 0.001$. (**D**) Schematic illustrations of hypothesized results showing higher density of E-E synapses with increasing memory strength. (**E**) Synaptic density of each connections. $n = 74$, context N-N; $n = 67$, context N-E; $n = 79$, weak N-N; $n = 80$, weak N-E; $n = 92$, strong N-N; $n = 91$, strong N-E; $n = 74$, context E-N; $n = 67$, context E-E; $n = 79$, weak E-N; $n = 80$, weak E-E; $n = 92$, strong E-N; $n = 91$, strong E-E. Fifteen images from six mice for context group. Sixteen images from five mice for weak group. Nineteen images from five mice for strong group. Mann-Whitney two-tailed test, n.s.: not significant, $^{*}P < 0.05$, $^{**}P < 0.01$, $^{***}P < 0.001$, $^{****}P < 0.0001$. (**F**) Spine head diameter of each connection. $n = 107$, context N-N; $n = 64$, context E-N; $n = 72$, weak N-N; $n = 34$, weak E-N; $n = 112$, strong N-N; $n = 46$, strong E-N; $n = 103$, context N-E; $n = 77$, context E-E; $n = 85$, weak N-E; $n = 84$, weak E-E; $n = 57$, strong N-E; $n = 110$, strong E-E, six mice for context group, five mice for weak shock group, five mice for strong shock group. Mann Whitney two-tailed test. n.s., not significant; $^{*}P < 0.05$, $^{**}P < 0.01$; $^{***}P < 0.001$; $^{****}P < 0.0001$. Data are represented as mean ± SEM.

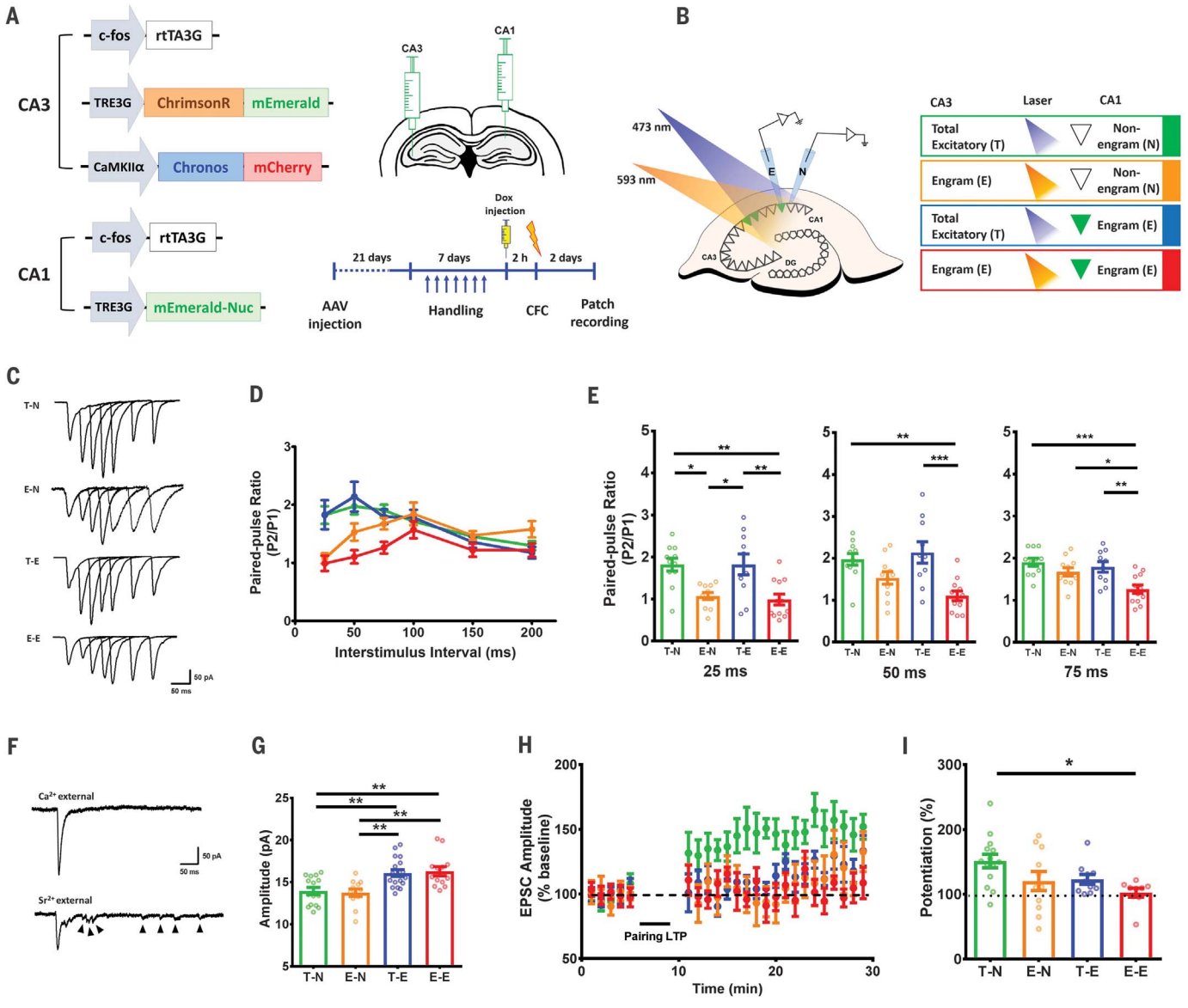

Fig. 4. Enhanced synaptic transmission between CA3 engram and CA1 engram cells through pre- and postsynaptic mechanisms. (**A**) (Left) Schematic illustration of injected AAVs. (Right) Illustration of virus injection sites and experimental protocol. (**B**) (Left) Diagram of whole-cell recording experiments. (Right) Classification of the four synaptic populations indicated by four colors. Green, T-N; orange, E-N; blue, T-E; red, E-E. The color for each group applies to all the panels below. (**C**) Traces from PPR recordings. (**D**) Results from PPR recordings. T-N, n = 11; T-E, n = 10; E-N, n = 11; E-E, n = 12. (**E**) Average PPR at the indicated interstimulus intervals. $^{*}P < 0.05$; $^{**}P < 0.01$; $^{***}P < 0.001$; Tukey's multiple comparison test after one-way ANOVA; (25 ms) $F(3,40) = 8.259$, $^{*}P = 0.0276$; (50 ms) $F(3,40) = 7.989$, $^{***}P = 0.0003$; (75 ms) $F(3,40) = 7.517$, $^{***}P = 0.0004$. (**F**) Traces of Sr^{2+} light-evoked mEPSCs. Arrowheads indicate quantal release events. (**G**) Average amplitude of the Sr^{2+} light-evoked mEPSCs. T-N, n = 15; T-E, n = 18; E-N, n = 12; E-E, n = 13; $^{**}P < 0.01$, Tukey's multiple comparison test after one-way ANOVA, $F(3,54) = 8.540$, $^{***}P < 0.0001$. (**H**) Pairing LTP with stimulus given after 5 min of baseline recording. T-N, n = 14; T-E, n = 10; E-N, n = 11; E-E, n = 9. (**I**) Average EPSC amplitude of the last 5 min of recording. $^{*}P < 0.05$, Tukey's multiple comparison test after one-way ANOVA, $F(3,40) = 3.683$, $^{*}P = 0.0197$. Data are represented as mean ± SEM.

(Fig. 4B). First, we investigated presynaptic transmission using paired-pulse ratios (PPR) (Fig. 4, C and D). PPR from CA3 engram inputs were significantly decreased at 25-, 50-, and 75-ms interstimulus intervals, which suggests increased release probability from CA3 engram inputs to CA1. The decrease was most prominent in E-E synaptic responses (Fig. 4E). We then examined postsynaptic α-amino-3-hydroxy-5-methyl-4-isoxazolepropionic acid (AMPA) receptor levels in individual synapses from the four combinations of synaptic responses by replacing Ca^{2+} with Sr^{2+} in the external recording solution (*26*, *27*). Sr^{2+} desynchronized evoked release and induced prolonged asynchronous release, which enabled measurement of quantal synaptic response (Fig. 4F). We measured the amplitude of evoked miniature excitatory postsynaptic currents (mEPSCs) 60 to 400 ms after light stimulation. Synapses from CA1 engram cells exhibited significantly increased levels of postsynaptic AMPA receptors compared with CA1 nonengram cell levels (Fig. 4G). These results indicate that the synapses of CA1 engram cells were potentiated after memory formation but not the synapses of CA1 nonengram cells. Alterations in both presynaptic release probability and postsynaptic potentiation are important for long-term

potentiation (LTP) (*28*). To measure the existence of LTP during memory formation, we examined the extent of LTP occlusion by inducing pairing LTP separately in the four synaptic types (Fig. 4H) (*29*). After 5 min of baseline recording, we delivered pairing LTP stimuli. We found robustly potentiated T-N synaptic responses (~150%). T-E and E-N synaptic responses were potentiated to a lower extent than T-N synaptic responses (~120%), but these differences were not significant. Interestingly, we found that pairing LTP in E-E synaptic responses was completely blocked and potentiation was significantly lower than T-N synaptic responses (Fig. 4I).

Our finding that synaptic populations that fired together during memory formation showed the strongest connections demonstrates that classical Hebbian plasticity indeed occurs during the learning and memory process at CA3 to CA1 synapses (*7*, *30*). It is possible that cells with higher connectivity are allocated together into a memory circuit, in contrast to enhanced connectivity after learning. However, the allocated cell number remains constant regardless of the memory strength, whereas the connectivity is significantly enhanced with a stronger memory. This finding indicates a significant contribution of post-learning enhancement over the predetermined connectivity. The relationship between memory strength and synaptic connectivity suggests that these specific connections between engram cells across two directly connected brain regions form the synaptic substrate for memory.

REFERENCES AND NOTES

1. C. A. Denny *et al*., *Neuron* **83**, 189–201 (2014).
2. J.-H. Han *et al*., *Science* **323**, 1492–1496 (2009).
3. X. Liu *et al*., *Nature* **484**, 381–385 (2012).
4. S. Ramirez *et al*., *Science* **341**, 387–391 (2013).
5. K. Z. Tanaka *et al*., *Neuron* **84**, 347–354 (2014).
6. Y. Zhou *et al*., *Nat. Neurosci.* **12**, 1438–1443 (2009).
7. D. O. Hebb, *The Organization of Behavior: A Neuropsychological Theory*. (Wiley, New York, NY, 1949).
8. J. Kim *et al*., *Nat. Methods* **9**, 96–102 (2011).
9. E. H. Feinberg *et al*., *Neuron* **57**, 353–363 (2008).
10. S. Cabantous, T. C. Terwilliger, G. S. Waldo, *Nat. Biotechnol.* **23**, 102–107 (2005).
11. M. T. Pisabarro, L. Serrano, *Biochemistry* **35**, 10634–10640 (1996).
12. J. Goedhart *et al*., *Nat. Commun.* **3**, 751 (2012).
13. M. L. Markwardt *et al*., *PLOS ONE* **6**, e17896 (2011).
14. R. M. Wachter, M.-A. Elsliger, K. Kallio, G. T. Hanson, S. J. Remington, *Structure* **6**, 1267–1277 (1998).
15. D. G. Amaral, H. E. Scharfman, P. Lavenex, *Prog. Brain Res.* **163**, 3–22 (2007).
16. G. T. Finnerty, J. G. Jefferys, *Neuroscience* **56**, 101–108 (1993).
17. L. G. Reijmers, B. L. Perkins, N. Matsuo, M. Mayford, *Science* **317**, 1230–1233 (2007).
18. G. van Haasteren, S. Li, S. Ryser, W. Schlegel, *Neuroendocrinology* **72**, 368–378 (2000).
19. X. Zhou, M. Vink, B. Klaver, B. Berkhout, A. T. Das, *Gene Ther.* **13**, 1382–1390 (2006).
20. R. Loew, N. Heinz, M. Hampf, H. Bujard, M. Gossen, *BMC Biotechnol.* **10**, 81 (2010).
21. D. S. Bindels *et al*., *Nat. Methods* **14**, 53–56 (2017).
22. D. M. Shcherbakova, V. V. Verkhusha, *Nat. Methods* **10**, 751–754 (2013).
23. D. J. Morrison *et al*., *Neurobiol. Learn. Mem.* **135**, 91–99 (2016).
24. N. C. Klapoetke *et al*., *Nat. Methods* **11**, 338–346 (2014).
25. J.-H. Choi *et al*., *Mol. Brain* **7**, 17 (2014).
26. F. A. Dodge Jr., R. Miledi, R. Rahamimoff, *J. Physiol.* **200**, 267–283 (1969).
27. M. A. Xu-Friedman, W. G. Regehr, *Biophys. J.* **76**, 2029–2042 (1999).
28. T. V. P. Bliss, G. L. Collingridge, *Mol. Brain* **6**, 5 (2013).
29. H.-X. Chen, N. Otmakhov, J. Lisman, *J. Neurophysiol.* **82**, 526–532 (1999).
30. N. Andersen, N. Krauth, S. Nabavi, *Curr. Opin. Neurobiol.* **45**, 188–192 (2017).

ACKNOWLEDGMENTS

Funding: This work was supported by the National Honor Scientist Program (NRF-2012R1A3A1050385) of Korea. C.S.L. was supported by the Basic Science Research Program (NRF-2016R1D1A1B03931525) through the National Research Foundation (NRF) of Korea. **Author contributions:** J.-H.C., S.-E.S., J.-i.K., and D.I.C. contributed equally to this work. J.-H.C. and B.K.K. designed the experiment, developed the dual-eGRASP and Fos-rtTA systems, and contributed to the analysis. S.-E.S. designed and performed all electrophysiology experiments and processed and analyzed the data. J.-i.K. produced and purified AAVs. J.-i.K. and D.I.C. performed viral injections, contextual fear conditioning, brain preparation, imaging, and analysis. J.O., J.L., C.S.L., S.Y., T.K., and H.-G.K assisted with viral injections, contextual fear conditioning, electrophysiology experiments, and analyzing data. B.K.K. supervised the project. J.-H.C., S.-E.S., J.-i.K., D.I.C., and B.K.K. wrote the manuscript. **Competing interests:** The authors declare no competing financial interests. **Data and materials availability:** All data to understand and assess the conclusions of this study are available in the main text or supplementary materials.

SUPPLEMENTARY MATERIALS

www.sciencemag.org/content/360/6387/430/suppl/DC1
Materials and Methods
Figs. S1 to S10
References (*31*, *32*)

4 January 2018; accepted 22 March 2018
10.1126/science.aas9204

Interregional synaptic maps among engram cells underlie memory formation

Jun-Hyeok Choi, Su-Eon Sim, Ji-il Kim, Dong Il Choi, Jihae Oh, Sanghyun Ye, Jaehyun Lee, TaeHyun Kim, Hyoung-Gon Ko, Chae-Seok Lim and Bong-Kiun Kaang

Science **360** (6387), 430-435.
DOI: 10.1126/science.aas9204

Memories are stored in synapses

Memory formation is thought to change the strength of synaptic connections between neurons. However, direct measurements between neurons that participate in a learning process are difficult to obtain. Choi *et al.* developed the "dual-eGRASP" technique to identify synaptic connections between hippocampal CA3 and CA1 pyramidal cells. This method could label two different sets of synapses so that their convergence on the same dendrites would be quantified. After contextual fear conditioning in mice, the number and size of spines were increased on CA1 engram cells receiving input from CA3 engram cells.

Science, this issue p. 430

Supplementary Materials for

Interregional synaptic maps among engram cells underlie memory formation

Jun-Hyeok Choi,* Su-Eon Sim,* Ji-il Kim,* Dong Il Choi,* Jihae Oh, Sanghyun Ye, Jaehyun Lee, TaeHyun Kim, Hyoung-Gon Ko, Chae-Seok Lim, Bong-Kiun Kaang†

*These authors contributed equally to this work.
†Corresponding author. Email: kaang@snu.ac.kr

Published 27 April 2018, *Science* **360**, 430 (2018)
DOI: 10.1126/aas9204

This PDF file includes:

Materials and Methods

Animals

All experiments were performed on 8~10-week-old male C57BL/6N mice purchased from Samtako. Bio. Korea. Mice were raised in 12-hr light/dark cycle in standard laboratory cages and given ad libitum access to food and water. All procedures and animal care followed the regulation and guidelines of the Institutional Animal Care and Use Committees (IACUC) of Seoul National University.

Construction of cyan and yellow eGRASP

The pre-eGRASP construct consists with an IgG kappa signal peptide, strand 1-10 of the mutant GFP, an Abl SH3 binding peptide and a neurexin1b stalk, transmembrane and intracellular domain. The strand 1-10 contains a S72A (amino acid numbering based on GFP sequence) mutation additionally to the original GRASP mutations. The cyan pre-eGRASP contains additional T65S, Y66W, H148G, T205S mutations including the S72A mutation, while yellow pre-eGRASP contains S72A and T203Y mutations. The Abl SH3 binding peptide was either p30 (APTKPPPLPP) or p32 (SPSYSPPPPP). Cyan pre-eGRASP with p30 and yellow pre-eGRASP with p32 were used in Figures 2, 3, S6, S8C, S8D, S9B, and S10 to overcome the relatively weaker expression of induced yellow pre-eGRASP compared to the constitutively expressed cyan pre-eGRASP. Pre-eGRASPs with p32 was used for the experiments in Figure 1 and Figure S8A and B, while p30 was used for the experiment in Figure S1D, S3. The post-eGRASP construct consists with an IgG kappa signal peptide, an Abl SH3 domain, strand 11 of the mutant GFP, and a neuroligin1 stalk, transmembrane and intracellular domain with the last 4 amino acids deleted. The last 4 amino acids of the neuroligin1 which consist the PDZ domain binding site were deleted to avoid undesired recruitment of scaffolding proteins and receptors. The protein sequence of each construct is listed below.

pre-eGRASP(p30) : IgG kappa signal peptide (orange), strand 1-10 with S72A mutation (green with green highlight for S72A), p30 (red), neurexin1b stalk, transmembrane and intracellular domain (blue). (p32 version has a replacement of APTKPPPLPP to SPSYSPPPPP)

METDTLLLWVLLLWVPGSTGDAPVGGSKGEELFTGVVPILVELDGDVNGHKFSV
RGEGEGDATIGKLTLKFICTTGKLPVPWPTLVTTLTYGVQCFARYPDHMKRHDF
FKSAMPEGYVQERTISFKDDGKYKTRAVVKFEGDTLVNRIELKGTDFKEDGNIL
GHKLEYNFNSHNVYITADKQKNGIKANFTVRHNVEDGSVQLADHYQQNTPIGD
GPVLLPDNHYLSTQTVLSKDPNEKTGGSGGSGGSRAPTKPPPLPPGGGSGGGSGT
EVPSSMTTESTATAMQSEMSTSIMETTTTLATSTARRGKPPTKEPISQTTDDILVA
SAECPSDDEDIDPCEPSSGGLANPTRVGGREPYPGSAEVIRESSSTTGMVVGIVAA
AALCILILLYAMYKYRNRDEGSYHVDESRNYISNSAQSNGAVVKEKQPSSAKSA
NKNKKNKDKEYYV

Cyan pre-eGRASP(p30) : IgG kappa signal peptide (orange), strand 1-10 with mutations (green with cyan highlights for cyan-specific mutated amino acids), p30 (red), neurexin1b stalk, transmembrane and intracellular domain (blue). (p32 version has a replacement of APTKPPPLPP to SPSYSPPPPP).

METDTLLLWVLLLWVPGSTGDAPVGGSKGEELFTGVVPILVELDGDVNGHKFSV
RGEGEGDATIGKLTLKFICTTGKLPVPWPTLVTTLSWGVQCFARYPDHMKRHDF
FKSAMPEGYVQERTISFKDDGKYKTRAVVKFEGDTLVNRIELKGTDFKEDGNIL
GHKLEYNFNSGNVYITADKQKNGIKANFTVRHNVEDGSVQLADHYQQNTPIGD
GPVLLPDNHYLSTQSVLSKDPNEKTGGSGGSGGSRAPTKPPPLPPGGGSGGGSGT
EVPSSMTTESTATAMQSEMSTSIMETTTTLATSTARRGKPPTKEPISQTTDDILVA
SAECPSDDEDIDPCEPSSGGLANPTRVGGREPYPGSAEVIRESSSTTGMVVGIVAA
AALCILILLYAMYKYRNRDEGSYHVDESRNYISNSAQSNGAVVKEKQPSSAKSA
NKNKKNKDKEYYV

Yellow pre-eGRASP(p30) : IgG kappa signal peptide (orange), strand 1-10 with mutations (green with yellow highlights for yellow-specific mutated amino acid), p30 (red), neurexin1b stalk, transmembrane and intracellular domain (blue). (p32 version has a replacement of APTKPPPLPP to SPSYSPPPPP)
METDTLLLWVLLLWVPGSTGDAPVGGSKGEELFTGVVPILVELDGDVNGHKFSV
RGEGEGDATIGKLTLKFICTTGKLPVPWPTLVTTLTYGVQCFARYPDHMKRHDF
FKSAMPEGYVQERTISFKDDGKYKTRAVVKFEGDTLVNRIELKGTDFKEDGNIL
GHKLEYNFNSHNVYITADKQKNGIKANFTVRHNVEDGSVQLADHYQQNTPIGD
GPVLLPDNHYLSYQTVLSKDPNEKTGGSGGSGGSRAPTKPPPLPPGGGSGGGSGT
EVPSSMTTESTATAMQSEMSTSIMETTTTLATSTARRGKPPTKEPISQTTDDILVA
SAECPSDDEDIDPCEPSSGGLANPTRVGGREPYPGSAEVIRESSSTTGMVVGIVAA
AALCILILLYAMYKYRNRDEGSYHVDESRNYISNSAQSNGAVVKEKQPSSAKSA
NKNKKNKDKEYYV

Post-eGRASP : IgG kappa signal peptide (orange), Abl SH3 domain (red), strand 11 (green), neuroligin1 stalk, transmembrane and intracellular domain with deletion (blue).
METDTLLLWVLLLWVPGSTGDAPVGGNDPNLFVALYDFVASGDNTLSITKGEKL
RVLGYNHNGEWCEAQTKNGQGWVPSNYITPVNSTGGGSGGGSGRDHMVLHEY
VNAAGITGGGSGGGSGTLELVPHLHNLNDISQYTSTTTKVPSTDITLRPTRKNSTP
VTSAFPTAKQDDPKQQPSPFSVDQRDYSTELSVTIAVGASLLFLNILAFAALYYK
KDKRRHDVHRRCSPQRTTTNDLTHAPEEEIMSLQMKHTDLDHECESIHPHEVVL
RTACPPDYTLAMRRSPDDIPLMTPNTITMIPNTIPGIQPLHTFNTFTGGQNNTLPHP
HPHPHSHS

Construction of Fos-rtTA system

Temporally-controlled activity dependent transgene expression uses a Fos promoter driven rtTA3G with an additional AU-rich element of Fos mRNA, which induces rapid destabilization of the mRNA following the rtTA3G. The transgene of interest is driven by a TRE3G promoter, making it both rtTA3G expression- and doxycycline-dependent.

Adeno-Associated Virus production

Adeno-Associated Viruses serotype 1/2 (AAV1/2; AAV particle that contains both serotype 1 and 2 capsids) were used in all the experiments. AAV1/2s were purified from HEK293T cells that were transfected with plasmids containing each expression cassette flaked by AAV2 ITRs, p5E18, p5E18-RXC1 and pAd-ΔF6 and cultured in 18 ml or 8 ml Opti-MEM (Gibco-BRL/Invitrogen, cat# 31985070) in a 150-mm or 100-mm culture

dish, respectively. Four days after transfection, the medium containing AAV1/2 particles was collected and centrifuged at 3,000 rpm for 10 min. After 1 ml of heparin-agarose suspension (Sigma, cat# H6508) was loaded onto a poly-prep chromatography column (Bio-Rad Laboratories, Inc. cat# 731-1550), the supernatant was loaded onto the column carefully. The column was washed by 4 ml of Buffer 4-150 (150 mM NaCl, pH4 10 mM citrate buffer) and 12 ml of Buffer 4-400 (400 mM NaCl, pH4 10 mM citrate buffer). The virus particles were eluted by 4 ml of Buffer 4-1200 (1.2 M NaCl, pH4 10 mM citrate buffer). The eluted solution was exchanged with PBS and concentrated using an Amicon Ultra-15 centrifugal filter unit (Millipore, cat# UFC910024). The titer was measured using quantitative RT-PCR.

Stereotaxic surgery

Mice (8~10 weeks) were anaesthetized with a ketamine/xylazine solution and positioned in a stereotaxic apparatus (Stoelting Co.). The virus was injected using 33 gauge needle with Hamilton syringe at a 0.1 μl/min rate into target regions. At all injected points, tip of the needle was positioned 0.05mm below the target coordinate and returned to the target site after 2min. After injection, the needle stayed in place for an additional 7 mins and was withdrawn slowly. Stereotaxic coordinates for each target sites: lateral entorhinal cortex (AP: -3.4/ ML: -4.4/ DV: -4.1), medial entorhinal cortex (AP: -4.6/ ML:-3.5/ DV-3.5), and DG (AP: -1.75/ ML: -1.5/ DV: -2.2 below from skull surface) for Fig. 1D; CA3 (AP: -1.9/ ML: ±2.35/ DV: -2.45) and CA1 (AP: -1.9/ ML: -1.5/ DV: -1.6) for Fig. 1E; left CA3 (AP: -1.75/ ML: -2.35/ DV: -2.45) and right CA1 (AP: -1.8/ ML: +1.5/ DV: -1.65 below the skull surface) for Fig. 2 and 3; left CA3 (double injection: AP: -1.75/ ML: -2.35/ DV: -2.45, AP: -2.25/ ML: -2.7/ DV: -2.65) and right CA1 (AP:-1.8/ ML:+1.5/ DV: -1.65 below the skull surface) for Fig. 4.

For Figure 2, 0.5 μl of a mixture of viruses ($1.6x10^6$ viral genome (vg)/μl of Fos-rtTA3G, $2.0x10^8$ vg/μl of TRE3G-Yellow pre-eGRASP, $4.0x10^7$ vg/μl of CaMKIIα-iCre, and $7.5x10^8$ vg/μl of EF1α-DIO-Cyan pre-eGRASP) was injected into left CA3. 0.5 μl of a mixture of viruses ($1.6x10^6$ vg/μl of Fos-rtTA3G, $8.0x10^9$ vg/μl of TRE3G-myr_mScarlet-I-P2A-post-eGRASP, $1.0x10^6$ vg/μl of CaMKIIα-iCre, $8.0x10^8$ vg/μl of EF1α-DIO-myr_iRFP670-P2A-post-eGRASP) was injected into right CA1. For Figure 3, 0.5 μl of a mixture of viruses ($1.6x10^6$ vg/μl of Fos-rtTA3G, $2.0x10^8$ vg/μl of TRE3G-Yellow pre-eGRASP, $3.0x10^7$ vg/μl of CaMKIIα-iCre, and $7.5x10^8$ vg/μl of EF1α-DIO-Cyan pre-eGRASP) was injected into left CA3. 0.5 μl of a mixture of viruses ($1.6x10^6$ vg/μl of Fos-rtTA3G, $8.0x10^9$ vg/μl of TRE3G-myr_mScarlet-I-P2A-post-eGRASP, $1.0x10^6$ vg/μl of CaMKIIα-iCre, $8.0x10^8$ vg/μl of EF1α-DIO-myr_iRFP670-P2A-post-eGRASP) was injected into right CA1. For Figure 4, 0.5 μl of a mixture of viruses ($2.0x10^7$ vg/μl Fos-rtTA3G, $3.37x10^9$ vg/μl of TRE3G-ChrimsonR-mEmerald, $1.0x10^8$ vg/μl of CaMKIIα-Chronos-mCherry) was injected into the left CA3. 0.5 μl of a mixture of viruses ($2.0x10^7$ vg/μl Fos-rtTA3G, $1.6x10^9$ vg/μl of TRE3G-mEmerald-Nuc) was injected into right CA1.

Contextual fear conditioning

All mice were conditioned 2~4 weeks after the AAV injection. Each mouse was single caged 10 days before conditioning and was habituated to the hands of the investigator and anesthesia chamber without isoflurane for 3 minutes on each of 7

consecutive days. Mice were conditioned 2 days after the last habituation day. On the conditioning day, 250 μl of 5 mg/ml Doxycycline solution dissolved in saline was injected by intraperitoneal injection during brief anesthesia by isoflurane in the anesthesia chamber 2 hours prior to the conditioning. Conditioning sessions used for Figure 2 were 300s in duration, and three 0.6 mA shocks of 2 s duration were delivered at 208 s, 238 s, and 268 s from the initiation of the session in a square chamber with a steel grid (Med Associates Inc., St Albans, VT). When the conditioning was finished, mice were immediately delivered to their homecage. 2 days after the conditioning, mice were carefully perfused for eGRASP signal analysis or decapitated for recording experiments respectively. Conditioning sessions to produce weak and strong memory for Figure 3 were 300 s in duration. One 0.35 mA and three 0.75 mA shocks of 2 s duration were delivered at 268 s and 208 s, 238 s, and 268 s respectively. Mice in the context only group were exposed to the same context during 300 s. 2 days after conditioning, mice were exposed to the same context to measure freezing levels and were carefully perfused for eGRASP signal analysis.

Sample preparation and confocal imaging

Perfused brains were fixed with 4% paraformaldehyde (PFA) in PBS overnight at 4℃ and dehydrated in 30% sucrose in PBS for 2 days at 4℃. After freezing, brains were sliced into 50μm sections by Cryostat and mounted in VECTASHIELD mounting medium (Vector Laboratories) or Easy-index mounting medium (Live Cell Instrument). CA1 apical dendritic regions of the brain slices were imaged by Leica SP8 or Zeiss LSM700 confocal microscope with 63x objectives with distilled water immersion. Secondary/tertiary dendrites of CA1 neurons were imaged in Z-stack.

Image analysis

We used Imaris (Bitplane, Zurich, Switzerland) software to process and reconstruct a 3D model of the confocal images. Each trackable myr_mScarlet-I-positive or myr_iRFP670-positive dendrite was denoted as a filament manually while hiding other 3 channels to exclude any bias by the investigator, and each cyan or yellow eGRASP signal was denoted as cyan or yellow sphere automatically. When the cyan and yellow eGRASP signals overlapped in a single synapse, it was denoted as a yellow spot as the presynaptic neuron of the synapse indicating IEG-positive during memory formation. Also, if a dendrite did not have any cyan eGRASP or if the myr_mScarlet-I and myr_iRFP670 signal overlapped in a single dendrite, the dendrite was not denoted as a filament for more accurate analysis.

For eGRASP density analysis, the numbers of denoted cyan and yellow spheres were manually counted along each denoted filaments. The length of each dendrite was measured using Imaris FilamentTracer. Cyan and yellow eGRASP density of each dendrite was normalized to the average density of the cyan and yellow eGRASP on the myr_iRFP670-positive dendrites, respectively, in each image. After denoting the trackable dendrites and eGRASP signals as the same way, eGRASP signal positive spines on denoted dendrites were reconstructed as 3D models and were measured using Imaris FilamentTracer. The investigator who reconstructed the spine 3D models was unaware of the color of the eGRASP signals. For memory strength experiments, the investigators who analyzed the images were unaware of the mouse group.

Electrophysiology

To improve slice conditions in adult hippocampal slices, we used *N*-methyl-D-glucamine (NMDG) solution (93 mM NMDG, 2.5 mM KCl, 1.2 mM NaH_2PO_4, 30 mM $NaHCO_3$, 20 mM HEPES, 25 mM Glucose, 5 mM sodium ascorbate, 2 mM Thiourea, 3 mM sodium pyruvate, 10 mM $MgSO_4$, 0.5 mM $CaCl_2$) for brain slicing and recovery (*31*). Mice were deeply anesthetized by intraperitoneal injection of Ketamine/Xylazine mixture and then transcardially perfused with ice-cold NMDG solution. Following cardiac perfusion, the coronal slices (300 ~ 400 μm thick) were prepared using a vibratome (VT1200S; Leica) in ice-cold NMDG solution, and then recovered in NMDG solution at 32 ~ 34 ℃ for 10 min. After recovery, the slices were transferred to modified HEPES holding ACSF (92 mM NaCl, 2.5 mM KCl, 1.2 mM NaH_2PO_4, 30 mM $NaHCO_3$, 20 mM HEPES, 25 mM Glucose, 5 mM sodium ascorbate, 2 mM Thiourea, 3 mM sodium pyruvate, 2 mM $MgSO_4$, 2 mM $CaCl_2$) at room temperature (RT) and allowed to recover for at least 1h. After recovery, the slice was transferred to the recording chamber constantly perfused with RT standard ACSF (124 mM NaCl, 2.5 mM KCl, 1 mM NaH_2PO_4, 25 mM $NaHCO_3$, 10 mM glucose, 2 mM $CaCl_2$, and 2 mM $MgSO_4$). The recording pipettes (3 ~ 5 MΩ) were filled with an internal solution containing (in mM) 145 K-gluconate, 5 NaCl, 10 HEPES, 1 $MgCl_2$, 0.2 EGTA, 2 MgATP, and 0.1 Na_3GTP (280 ~ 300 mOsm, adjust to pH 7.2 with KOH). Picrotoxin (100 μM) was added to the ACSF to block the GABA-R-mediated currents. Blue light was delivered by 473 nm DPSS laser (Laserglow Technologies Inc.) and yellow light was delivered by 593 nm DPSS laser (OEM Laser Systems). Light intensity was adjusted to elicit a reliable synaptic response (*32*). For Sr^{2+} light-evoked mEPSC experiments, we used modified ACSF containing 4 mM $MgCl_2$ and 4 mM $SrCl_2$ instead of $CaCl_2$. Light was delivered for a duration of 300 ms. To exclude the synchronous release component, mEPSC events in 60 ~ 400 ms post light stimulation were analyzed by MiniAnalysis program (Synaptosoft). For pairing-LTP experiments, EPSCs were evoked at 0.05 Hz and three successive EPSCs were averaged and expressed relative to the normalized baseline. To induce pairing-LTP, four brief high-frequency tetani (50 pulse of 20 Hz per each; 4 s intervals) paired with a long depolarization (3 min to 0 mV) given at the end of the long depolarization. Hippocampal neurons were voltage-clamped at -70 mV using an Axopatch 200B (Molecular Devices). Only cells with a change in access resistance < 20% were included in the analysis. mEmerald-nuc expression was confirmed by a cooled CCD camera (ProgRes MF cool; Jenoptik) and fluorescence microscope (BX51WI; Olympus).

Statistical analysis

Data were analyzed using Prism software. Mann Whitney two-tailed test and Tukey's multiple comparison test after one-way ANOVA were used to test for statistical significance when applicable. The exact value of n and statistical significance are reported in each figure legends.

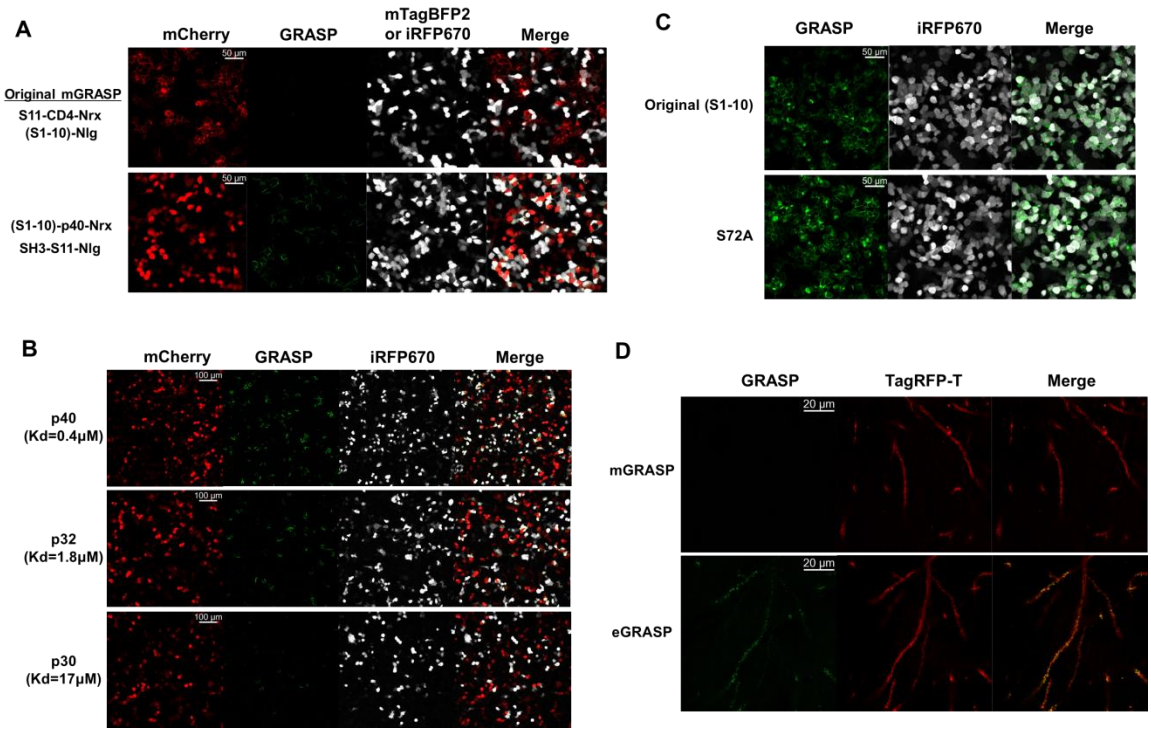

Fig. S1. Enhancement of GRASP signal.

(A) (Top) Either post-mGRASP with mTagBFP2 coexpression or pre-mGRASP with mCherry fusion was transfected separately in HEK293T cells by nucleofection. The interface of mCherry positive cell and mTagBFP2 positive cell shows only faint GRASP signal, only detectable when exposed to stronger excitation. (Bottom) Either post-eGRASP (SH3-S11-Nlg) with iRFP670 coexpression or (S1-10)-p40-Nrx with mCherry coexpression was transfected separately in HEK293T cells by nucleofection. Peptide p40 (APTYSPPPPP) binds to the SH3 domain in the post-eGRASP construct enhancing the GRASP signal. The interface of a mCherry positive cell and an iRFP670 positive cell shows strong GRASP signal. (B) Exchanging the SH3 binding peptide to those with lower interacting strength reduces the GRASP signal, while still showing significant GRASP signal compared to mGRASP. The known dissociation constants for SH3 domain and each peptide are indicated below the peptide. (C) Additional S72A mutation on the strand 1-10 of the split GFP increase the GRASP signal. (D) (Top) pre-mGRASP was expressed in the CA3 and post-mGRASP with membrane-targeted TagRFP-T was expressed sparsely in CA1. (Bottom) pre-eGRASP with the weakest interacting peptide (p30) was expressed in CA3 and post-eGRASP with membrane-targeted TagRFP-T was expressed sparsely in CA1. mGRASP signal was not detectable in our condition, while the eGRASP signal was clearly visible on the spines of CA1 dendrites even with the weakest interacting peptide.

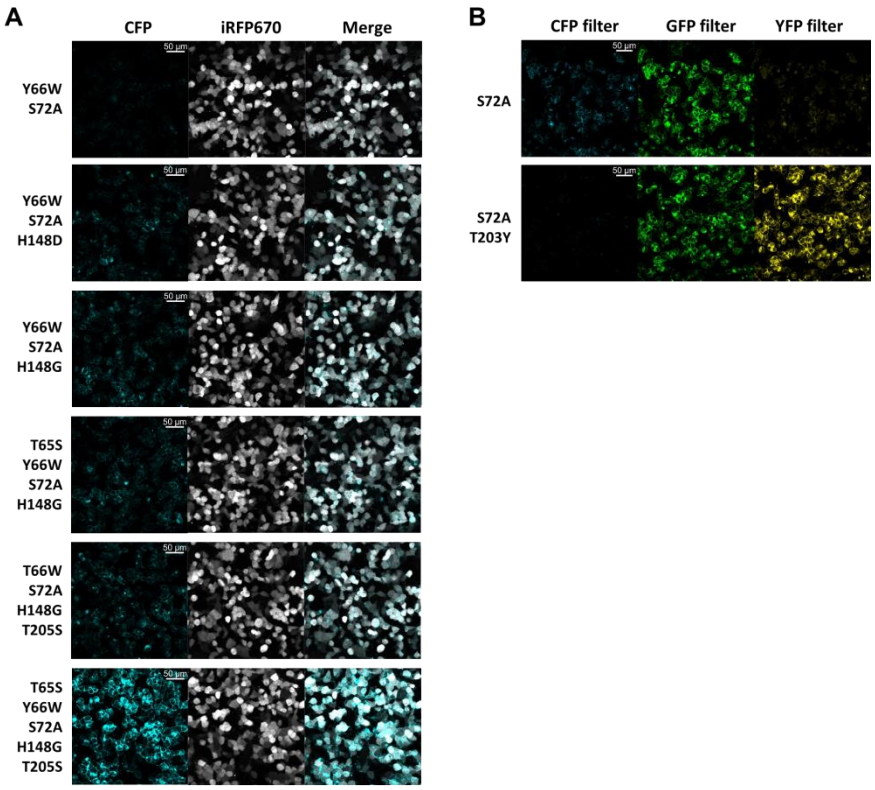

Fig. S2. Development of cyan and yellow eGRASP.

(A) Pre-eGRASP with indicated mutations, post-eGRASP and iRFP670 were coexpressed in HEK293T cells. Pre-eGRASP that contains T65S, Y66W, S72A, H148G, T205S shows the brightest cyan fluorescence. (B) Pre-eGRASP with indicated mutations, post-eGRASP and iRFP670 were coexpressed in HEK293T cells. Pre-eGRASP that contains S72A, T203Y shows bright signal detected in both the GFP and YFP filters, but not in the CFP filter. The original pre-eGRASP shows signal using every filter with the GFP filter being the brightest. This indicates that the T203Y mutation results in red shifted fluorescence that is separable from the CFP signal.

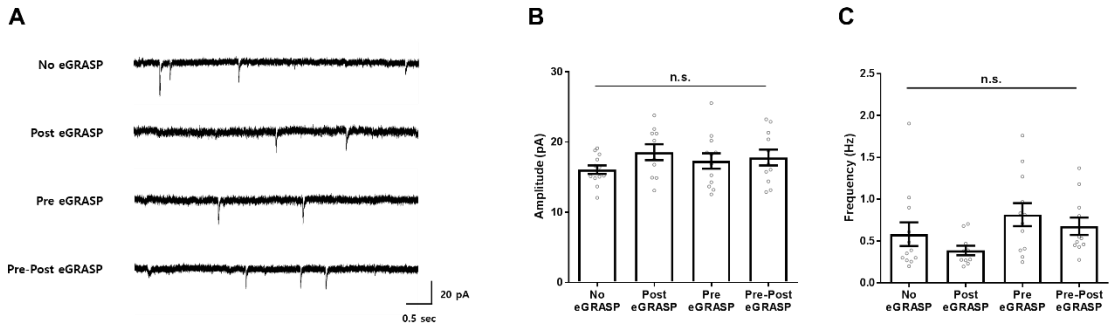

Fig. S3. Expression of dual-eGRASP components has no effects on basal synaptic transmission.

(A) Representative miniature EPSC (mEPSC) recording traces. (B and C) Amplitude and frequency of mEPSCs from CA1 pyramidal neurons in slices expressing eGRASP components in CA3 and CA1 as indicated in each group. No eGRASP (no eGRASP components in both CA3 and CA1), n = 12; Post eGRASP (post-eGRASP in CA1), n = 10; Pre eGRASP (pre-eGRASP in CA3), n = 12; Pre-Post eGRASP (pre-eGRASP in CA3 and post-eGRASP in CA1), n = 11. One-way ANOVA of amplitude, n.s.: not significant, $F(3,41) = 1.074$, $p = 0.3705$. One-way ANOVA of frequency, n.s.: not significant, $F(3,41) = 2.167$, $p = 0.1065$. Data are represented as mean ± SEM.

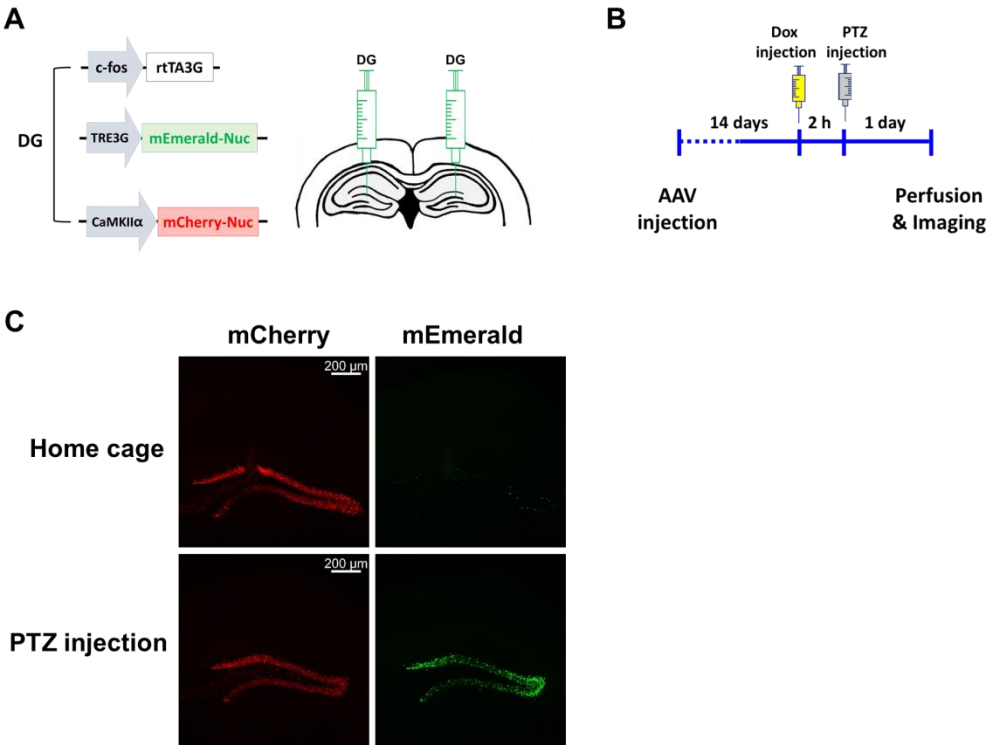

Fig. S4. Validation of Fos-rtTA system with seizure.

(A) Schematic illustration of injected AAVs. Nucleus-targeted mEmerald (mEmerald-Nuc) was driven by the TRE3G promoter controlled by Fos promoter-driven rtTA3G. CaMKIIα driven nucleus targeted mCherry was used as an expression control. (B) Behavioral schedule used in the experiments. (C) Seizure-inducing Pentylenetetrazol (PTZ) injection induces a strong mEmerald-Nuc signal in the DG.

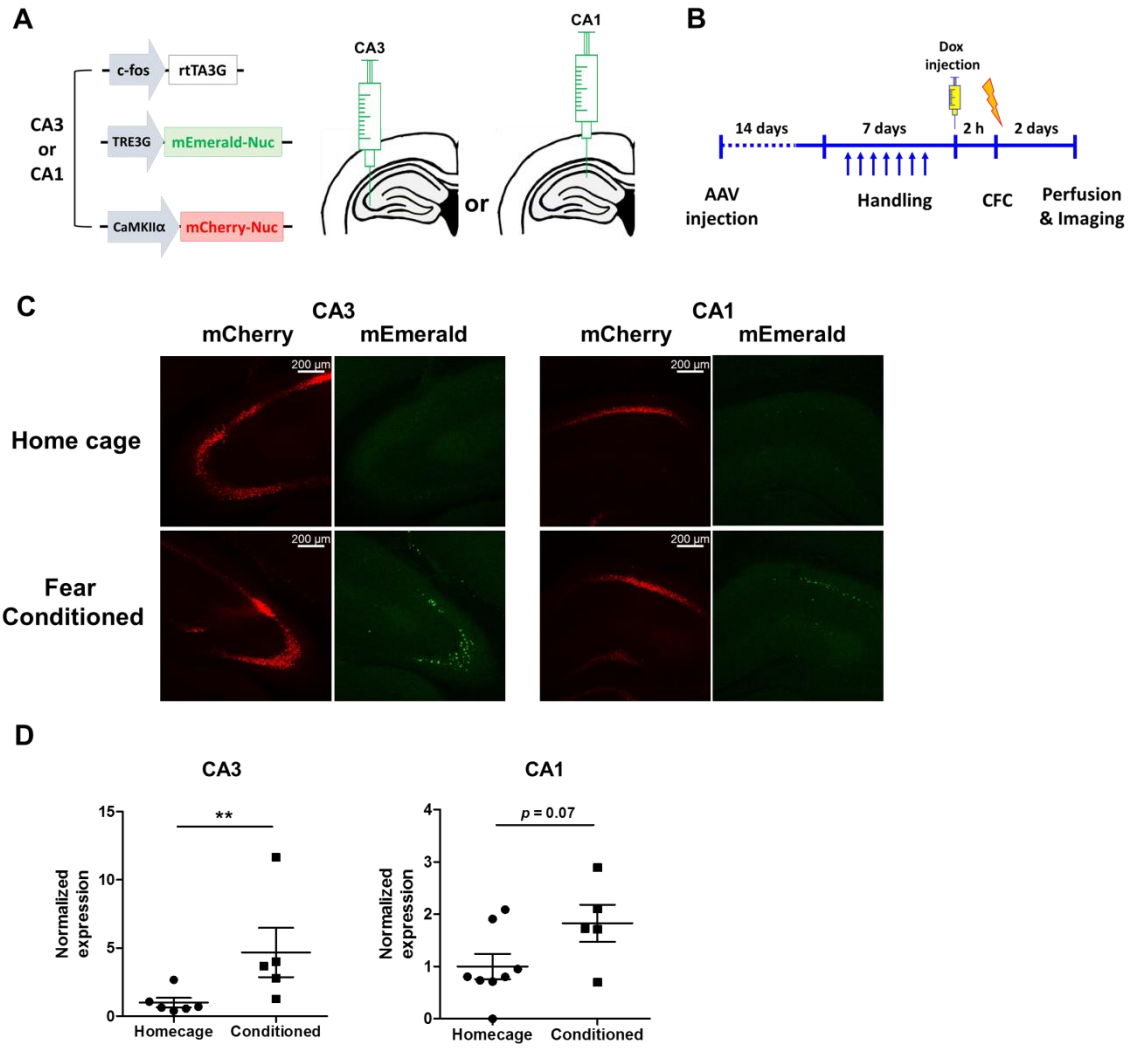

Fig. S5. Validation of Fos-rtTA system on contextual fear conditioning.

(A) Schematic illustration of injected AAVs. (B) Behavioral schedule used in the experiments. (C) Representative images. (D) Fear conditioning induces significant increase of mEmerald-Nuc in the CA3 and a strong tendency of increase in the CA1. n = 6, CA3 Homecage; n = 5, CA3 Conditioned; n = 8, CA1 Homecage; n = 5, CA1 Conditioned. Unpaired two-tailed t test, **p < 0.01. Data are represented as mean ± SEM.

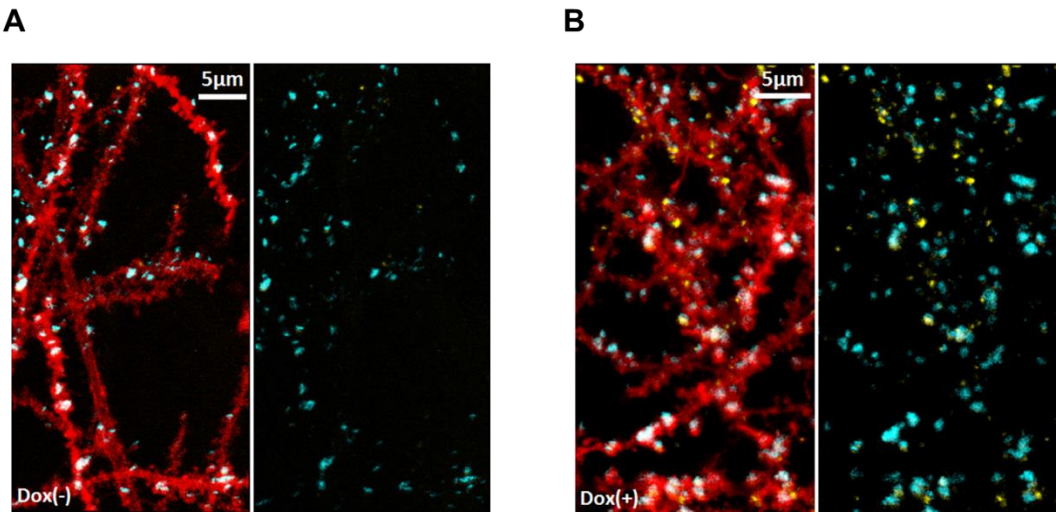

Fig. S6. Validation of Yellow eGRASP expression control by doxycycline.
(A and B) Representative images of cyan and yellow eGRASP expression without doxycycline (A) or with doxycycline injection (B). myrTagRFP-T-P2A-post-eGRASP, as well as cyan pre-eGRASP, was expressed constitutively using the DIO/Cre system to express each construct in random populations of CA1 and CA3 neurons, while yellow pre-eGRASP was expressed in CA3 through the Fos-rtTA system.

A

	on iRFP670 dendrite
cyan & yellow overlap / cyan	40.25 %
cyan & yellow overlap / yellow	78.38 %

B

	on mScarlet-I dendrite
cyan & yellow overlap / cyan	50.00 %
cyan & yellow overlap / yellow	80.37%

C

iRFP670 & mScarlet-I overlap / iRFP670	20.93 %
iRFP670 & mScarlet-I overlap / mScarlet-I	11.61%

Fig. S7. Overlapping percentage of neuronal populations.
(A) The percentage of cyan signal that also contains yellow signal on iRFP670 positive dendrites is 40.25 %. The percentage of yellow signal that also contains cyan signal on iRFP670 positive dendrites is 78.38 %. n=43. 43 iRFP670 dendrites from 3 mice. (B) The percentage of cyan signal that also contains yellow signal on mScarlet-I positive dendrites is 50.00 %. The percentage of yellow signal that also contains cyan signal on mScarlet-I positive dendrites is 80.37 %, n=45, 45 mScarlet-I dendrites from 3 mice. (C) The percentage of iRFP670 positive cells that also express mScarlet-I is 20.93 %. The percentage of mScarlet-I positive cells that also express iRFP670 is 11.61 %. n=10, 10 CA1 cell layer images from 3 mice.

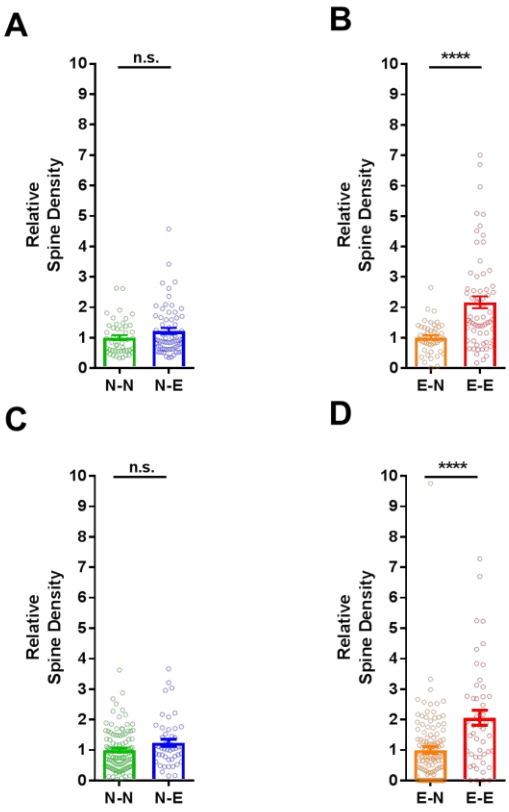

Fig. S8. Effect of different interaction strength on synaptic density.
(A and B) Synaptic density for N-N synapses is comparable with N-E synapses. However, synaptic density for E-E synapses is significantly higher than E-N synapses. Each data point represents a dendrite. n = 47 for CA1 non-engram dendrites, and n = 64 for CA1 engram dendrites, 11 images from 5 mice, Mann Whitney two-tailed test, n.s.: not significant, ****p < 0.0001. The interacting peptides for both cyan and yellow eGRASP are p32. The experimental design was identical as Figure 2 except that the red fluorescent protein was TagRFP-T instead of mScarlet-I. (C and D) Synaptic density for N-N synapses is comparable with N-E synapses. However, synaptic density for E-E synapses is significantly higher than E-N synapses. Each data point represents a dendrite. n = 116 for CA1 non-engram dendrites, n = 48 for CA1 engram dendrites, 9 images from 4 mice, Mann Whitney two-tailed test, n.s.: not significant, ****p < 0.0001. The interacting peptide for cyan is p30, while p32 was used for yellow eGRASP. The experimental design was identical as Figure 2 except that the red fluorescent protein was TagRFP-T instead of mScarlet-I. Data are represented as mean ± SEM.

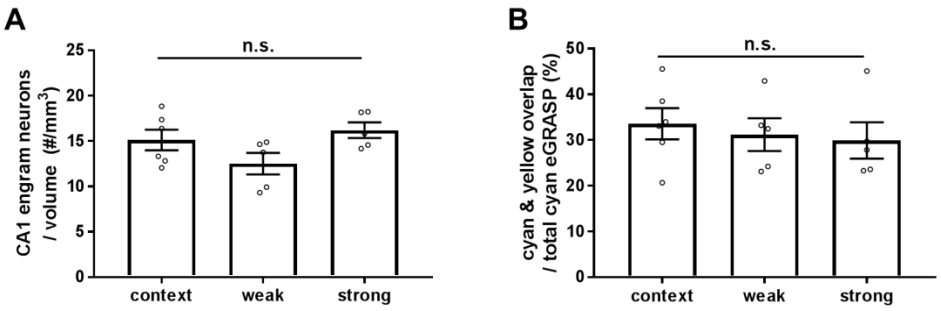

Fig. S9. Comparable number of CA3 and CA1 engram cells across the different memory strength.

(A) The number of CA1 engram neurons expressing myr_mScarlet-I was constant among three groups. context, n = 6; weak, n = 5; strong, n = 5, one-way ANOVA, n.s.: not significant, $F(2,13) = 2.872$, $p = 0.0927$. (B) The number of CA3 engram neurons estimated through the percentage of yellow eGRASP signal overlapping on cyan eGRASP signal was constant among three groups. context, n = 6; weak, n = 5; strong, n = 5. one-way ANOVA, n.s.: not significant, $F(2,13) = 0.264$, $p = 0.7720$. Data are represented as mean ± SEM.

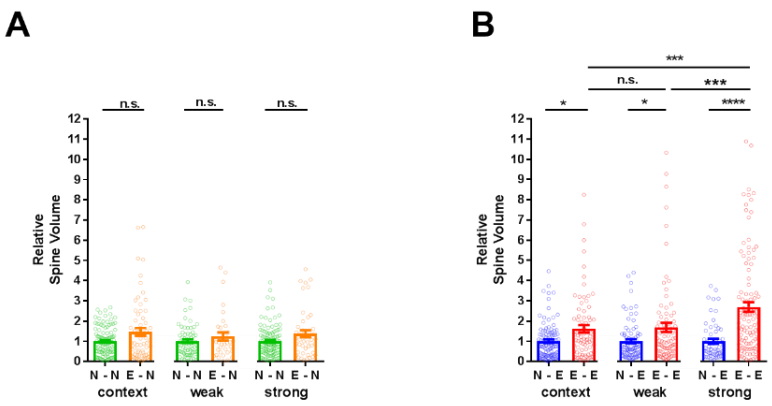

Fig. S10. Spine volume between pre- and post-engram cells is correlated to memory strength.

(A) Comparable spine volume between N-N spines and E-N spines in all groups. (B) The degree of enhancement of spine volume for E-E spines by conditioning is significantly higher in strong group than that in weak and context groups. (A and B) Each data point represents a spine. n = 107, context N-N; n = 64, context E-N; n = 72, weak N-N; n = 34, weak E-N; n = 112, strong N-N; n = 46, strong E-N; n = 103, context N-E; n = 77, context E-E; n = 85, weak N-E; n = 84, weak E-E; n = 57, strong N-E; n = 110, strong E-E, 6 mice for context group, 5 mice for weak group, 5 mice for strong group. Mann Whitney two-tailed test, n.s.: not significant, *$p < 0.05$, **$p < 0.01$, ***$p < 0.001$, ****$p < 0.0001$. Data are represented as mean ± SEM.

References

1. C. A. Denny, M. A. Kheirbek, E. L. Alba, K. F. Tanaka, R. A. Brachman, K. B. Laughman, N. K. Tomm, G. F. Turi, A. Losonczy, R. Hen, Hippocampal memory traces are differentially modulated by experience, time, and adult neurogenesis. *Neuron* **83**, 189–201 (2014). doi:10.1016/j.neuron.2014.05.018 Medline

2. J.-H. Han, S. A. Kushner, A. P. Yiu, H.-L. Hsiang, T. Buch, A. Waisman, B. Bontempi, R. L. Neve, P. W. Frankland, S. A. Josselyn, Selective erasure of a fear memory. *Science* **323**, 1492–1496 (2009). doi:10.1126/science.1164139 Medline

3. X. Liu, S. Ramirez, P. T. Pang, C. B. Puryear, A. Govindarajan, K. Deisseroth, S. Tonegawa, Optogenetic stimulation of a hippocampal engram activates fear memory recall. *Nature* **484**, 381–385 (2012). Medline

4. S. Ramirez, X. Liu, P.-A. Lin, J. Suh, M. Pignatelli, R. L. Redondo, T. J. Ryan, S. Tonegawa, Creating a false memory in the hippocampus. *Science* **341**, 387–391 (2013). doi:10.1126/science.1239073 Medline

5. K. Z. Tanaka, A. Pevzner, A. B. Hamidi, Y. Nakazawa, J. Graham, B. J. Wiltgen, Cortical representations are reinstated by the hippocampus during memory retrieval. *Neuron* **84**, 347–354 (2014). doi:10.1016/j.neuron.2014.09.037 Medline

6. Y. Zhou, J. Won, M. G. Karlsson, M. Zhou, T. Rogerson, J. Balaji, R. Neve, P. Poirazi, A. J. Silva, CREB regulates excitability and the allocation of memory to subsets of neurons in the amygdala. *Nat. Neurosci.* **12**, 1438–1443 (2009). doi:10.1038/nn.2405 Medline

7. D. O. Hebb, *The Organization of Behavior: A Neuropsychological Theory*. (Wiley, New York, NY, 1949).

8. J. Kim, T. Zhao, R. S. Petralia, Y. Yu, H. Peng, E. Myers, J. C. Magee, mGRASP enables mapping mammalian synaptic connectivity with light microscopy. *Nat. Methods* **9**, 96–102 (2011). doi:10.1038/nmeth.1784 Medline

9. E. H. Feinberg, M. K. Vanhoven, A. Bendesky, G. Wang, R. D. Fetter, K. Shen, C. I. Bargmann, GFP reconstitution across synaptic partners (GRASP) defines cell contacts and synapses in living nervous systems. *Neuron* **57**, 353–363 (2008). doi:10.1016/j.neuron.2007.11.030 Medline

10. S. Cabantous, T. C. Terwilliger, G. S. Waldo, Protein tagging and detection with engineered self-assembling fragments of green fluorescent protein. *Nat. Biotechnol.* **23**, 102–107 (2005). doi:10.1038/nbt1044 Medline

11. M. T. Pisabarro, L. Serrano, Rational design of specific high-affinity peptide ligands for the Abl-SH3 domain. *Biochemistry* **35**, 10634–10640 (1996). doi:10.1021/bi960203t Medline

12. J. Goedhart, D. von Stetten, M. Noirclerc-Savoye, M. Lelimousin, L. Joosen, M. A. Hink, L. van Weeren, T. W. J. Gadella Jr., A. Royant, Structure-guided evolution of cyan fluorescent proteins towards a quantum yield of 93%. *Nat. Commun.* **3**, 751 (2012). doi:10.1038/ncomms1738 Medline

13. M. L. Markwardt, G.-J. Kremers, C. A. Kraft, K. Ray, P. J. C. Cranfill, K. A. Wilson, R. N. Day, R. M. Wachter, M. W. Davidson, M. A. Rizzo, An improved cerulean fluorescent

protein with enhanced brightness and reduced reversible photoswitching. *PLOS ONE* **6**, e17896 (2011). doi:10.1371/journal.pone.0017896 Medline

14. R. M. Wachter, M.-A. Elsliger, K. Kallio, G. T. Hanson, S. J. Remington, Structural basis of spectral shifts in the yellow-emission variants of green fluorescent protein. *Structure* **6**, 1267–1277 (1998). doi:10.1016/S0969-2126(98)00127-0 Medline

15. D. G. Amaral, H. E. Scharfman, P. Lavenex, The dentate gyrus: Fundamental neuroanatomical organization (dentate gyrus for dummies). *Prog. Brain Res.* **163**, 3–22 (2007). doi:10.1016/S0079-6123(07)63001-5 Medline

16. G. T. Finnerty, J. G. Jefferys, Functional connectivity from CA3 to the ipsilateral and contralateral CA1 in the rat dorsal hippocampus. *Neuroscience* **56**, 101–108 (1993). doi:10.1016/0306-4522(93)90566-X Medline

17. L. G. Reijmers, B. L. Perkins, N. Matsuo, M. Mayford, Localization of a stable neural correlate of associative memory. *Science* **317**, 1230–1233 (2007). doi:10.1126/science.1143839 Medline

18. G. van Haasteren, S. Li, S. Ryser, W. Schlegel, Essential contribution of intron sequences to Ca^{2+}-dependent activation of *c-fos* transcription in pituitary cells. *Neuroendocrinology* **72**, 368–378 (2000). doi:10.1159/000054606 Medline

19. X. Zhou, M. Vink, B. Klaver, B. Berkhout, A. T. Das, Optimization of the Tet-On system for regulated gene expression through viral evolution. *Gene Ther.* **13**, 1382–1390 (2006). doi:10.1038/sj.gt.3302780 Medline

20. R. Loew, N. Heinz, M. Hampf, H. Bujard, M. Gossen, Improved Tet-responsive promoters with minimized background expression. *BMC Biotechnol.* **10**, 81 (2010). doi:10.1186/1472-6750-10-81 Medline

21. D. S. Bindels, L. Haarbosch, L. van Weeren, M. Postma, K. E. Wiese, M. Mastop, S. Aumonier, G. Gotthard, A. Royant, M. A. Hink, T. W. J. Gadella Jr., mScarlet: A bright monomeric red fluorescent protein for cellular imaging. *Nat. Methods* **14**, 53–56 (2017). doi:10.1038/nmeth.4074 Medline

22. D. M. Shcherbakova, V. V. Verkhusha, Near-infrared fluorescent proteins for multicolor in vivo imaging. *Nat. Methods* **10**, 751–754 (2013). doi:10.1038/nmeth.2521 Medline

23. D. J. Morrison, A. J. Rashid, A. P. Yiu, C. Yan, P. W. Frankland, S. A. Josselyn, Parvalbumin interneurons constrain the size of the lateral amygdala engram. *Neurobiol. Learn. Mem.* **135**, 91–99 (2016). doi:10.1016/j.nlm.2016.07.007 Medline

24. N. C. Klapoetke, Y. Murata, S. S. Kim, S. R. Pulver, A. Birdsey-Benson, Y. K. Cho, T. K. Morimoto, A. S. Chuong, E. J. Carpenter, Z. Tian, J. Wang, Y. Xie, Z. Yan, Y. Zhang, B. Y. Chow, B. Surek, M. Melkonian, V. Jayaraman, M. Constantine-Paton, G. K.-S. Wong, E. S. Boyden, Independent optical excitation of distinct neural populations. *Nat. Methods* **11**, 338–346 (2014). doi:10.1038/nmeth.2836 Medline

25. J.-H. Choi, N.-K. Yu, G.-C. Baek, J. Bakes, D. Seo, H. J. Nam, S. H. Baek, C.-S. Lim, Y.-S. Lee, B.-K. Kaang, Optimization of AAV expression cassettes to improve packaging capacity and transgene expression in neurons. *Mol. Brain* **7**, 17 (2014). doi:10.1186/1756-6606-7-17 Medline

26. F. A. Dodge Jr., R. Miledi, R. Rahamimoff, Strontium and quantal release of transmitter at the neuromuscular junction. *J. Physiol.* **200**, 267–283 (1969). doi:10.1113/jphysiol.1969.sp008692 Medline

27. M. A. Xu-Friedman, W. G. Regehr, Presynaptic strontium dynamics and synaptic transmission. *Biophys. J.* **76**, 2029–2042 (1999). doi:10.1016/S0006-3495(99)77360-1 Medline

28. T. V. P. Bliss, G. L. Collingridge, Expression of NMDA receptor-dependent LTP in the hippocampus: Bridging the divide. *Mol. Brain* **6**, 5 (2013). doi:10.1186/1756-6606-6-5 Medline

29. H.-X. Chen, N. Otmakhov, J. Lisman, Requirements for LTP induction by pairing in hippocampal CA1 pyramidal cells. *J. Neurophysiol.* **82**, 526–532 (1999). doi:10.1152/jn.1999.82.2.526 Medline

30. N. Andersen, N. Krauth, S. Nabavi, Hebbian plasticity in vivo: Relevance and induction. *Curr. Opin. Neurobiol.* **45**, 188–192 (2017). doi:10.1016/j.conb.2017.06.001 Medline

31. J. T. Ting, T. L. Daigle, Q. Chen, G. Feng, Acute brain slice methods for adult and aging animals: Application of targeted patch clamp analysis and optogenetics. *Methods Mol. Biol.* **1183**, 221–242 (2014). doi:10.1007/978-1-4939-1096-0_14 Medline

32. S. J. Kang, C. Kwak, J. Lee, S.-E. Sim, J. Shim, T. Choi, G. L. Collingridge, M. Zhuo, B.-K. Kaang, Bidirectional modulation of hyperalgesia via the specific control of excitatory and inhibitory neuronal activity in the ACC. *Mol. Brain* **8**, 81 (2015). doi:10.1186/s13041-015-0170-6 Medline